Coastal Upwelling and Estuarine Gravitational Circulation: A Feedback System in a Tropical Estuary in the South Atlantic

Lucas S. Fonseca[1] · Guilherme C. Lessa[1] · Martinho Marta-Almeida[2] · Carlos Eduardo P. Teixeira[3]

Abstract

This study examines the effects of coastal upwelling on the longitudinal water density gradient within the estuary of Baía de Todos os Santos (BTS), its effect on the gravitational circulation at the estuary entrance, and the reverse effect of gravitational circulation on the coastal upwelling. This investigation was based on a 1-year dataset of observed water temperature, mean velocities, and river discharge, as well as 2 years of numerical simulation of the estuarine flow. The results show that the upwelling regulates the thermohaline field in front of the BTS, decreasing water temperature (up to 3 °C), and increasing density (up to 0.3 kg/m^3), and have sufficient intensity to more than double the speed, or even establish, the gravitational circulation. It was frequently observed that the water temperature falls after an increase in the subtidal flow shear, suggesting that the estuarine gravitational circulation acts as a facilitator to the upwelling process. Numerical simulations indicate that the coastal upwelling events are also capable of reestablishing the gravitational circulation at times with weak longitudinal density gradient, a scenario that tends to become more frequent and intense in the near future due to the ongoing climate changes.

Keywords Baía de Todos os Santos · Coastal circulation · Water density · Climate change

Introduction

Longitudinal density gradients in estuaries can drive sheared tide-averaged flows, namely gravitational circulation, and expedite the estuary-shelf exchanges (Geyer and MacCready 2014; Giddings and MacCready 2017). The density gradients driving the gravitational circulation are commonly ascribed to fluvial discharges and spatial variations in temperature (De Silva Samarasinghe et al. 2003; Hansen and Rattray 1965; Santana et al. 2018). However, hydrographic changes of shelf water, induced by higher river discharges updrift (Giddings and MacCready 2017; Juarez et al. 2020) and coastal upwelling (Barton et al. 2015; Duxbury 1979; Giddings and

MacCready 2017; Gilcoto et al. 2017; Harcourt-Baldwin and Diedericks 2006; Hickey et al. 2002; Sun et al. 2018), can also affect the along-estuary density gradients and influence the gravitational circulation. The presence of upwelled waters, with lower temperature and higher salinity, on the shelf increases the longitudinal density gradient and strengthens the vertical shear, and may even become the sole feature responsible for the gravitational circulation in low inflow estuaries subjected to dry summers (Harcourt-Baldwin and Diedericks 2006; Monteiro and Largier 1999).

Investigations addressing the upwelling impact on the gravitational circulation, or the upwelling effect upon the estuarine hydrography (Monteiro and Largier 1999; Valle-Levinson et al. 2003), were carried out on mid-latitudes of the eastern ocean margins, where upwelling processes are notoriously vigorous and promote sharper thermal (density) gradients between warmer estuarine and colder shelf waters (Monteiro and Largier 1999). Although coastal upwelling has also been documented in tropical regions and on western ocean margins (Berkelmans et al. 2010; Rueda-Roa and Muller-Karger 2013; Thévenin et al. 2019), the investigation of its impact on the estuarine circulation is probably restricted to the study by Sun et al. (2018) on the upwelling-forced gravitational circulation in sub-tropical Jervis Bay, on the eastern Australia coast.

✉ Guilherme C. Lessa
gclessa@gmail.com

1　Post-Graduate Program in Geophysics, Federal University of Bahia, Salvador, Brazil

2　Centro Oceanográfico de A Coruña, Instituto Español de Oceanografia (IEO-CSIC), A Coruña, Spain

3　Instituto de Ciências do Mar, Universidade Federal do Ceará, Fortaleza, Brazil

Thévenin et al. (2019) showed that strong Ekman processes around 12°S on the Brazilian coast cause temperature anomalies greater than –2 °C on a narrow (~ < 10 km wide) continental shelf. These events occur in the austral springs and summers and encompass an area frontal to Baía de Todos os Santos (BTS), a tectonic estuary where vertically sheared subtidal flow occur throughout the year both inside the estuary and across the narrow continental shelf (Aguiar et al. 2019; Lessa et al. 2018; Thévenin et al. 2019). According to the understanding of the bay dynamics to date (Aguiar et al. 2019; Cirano and Lessa 2007; Lessa et al. 2018; Santana et al. 2018), the sheared flow is forced by density gradients set up by fluvial discharges and by the seasonal change in water temperature inside the bay. Both drivers act synchronously to enhance the longitudinal density gradient in the summer, when the water temperature inside the bay and the flow of its largest tributary are the highest. Therefore, the arrival of cooler shelf water at the bay entrance concurrent with the occurrence of warmer and less dense waters inside the bay should boost the gravitational circulation. Likewise, mass continuity suggests that an extension of the vertically sheared estuarine flow across the narrow shelf impacts the ocean-shelf exchange, or the upwelling process itself. For instance, Lü et al. (2006) showed that the gravitational circulation induced by the Yangtsé River flow on the shelf is a main driver for coastal upwelling in a region where the wind is unfavorable to the process.

It is the aim of this study to investigate, by means of observational data and numerical simulations, (i) the importance of upwelling events on the reinforcement and maintenance of the gravitational circulation along the entrance channel of BTS, and (ii) the existence of a feedback mechanism between the estuarine gravitational circulation and the local upwelling.

Methods

A set of observed, remotely sensed, and numerically modeled data obtained inside the estuary and adjoining shelf was used in this study. The investigation was centered between November 2014 and January 2015, when there were significant upwelling events, high river discharges, and large temperature gradients between the shelf and the estuary. In order to investigate whether the coastal upwelling can establish gravitational circulation on its own, numerically modeled data from the summer/autumn of 2013, when longitudinal density gradients were very small or non-existent, will also be explored.

Observed Data

Water velocity, temperature, and level were obtained with upward-looking Teledyne-RDI 600 MHz ADCP's

deployed on the shelf (stations #A0 and #A1) and in Salvador Channel (station #A2 in Fig. 1) between November 2014 and October 2015 at about 30 m of depth. The ADCP at #A0 was configured to record 2-min averages every hour (sampling at 1 Hz), whereas those at #A1 and #A2 recorded 2-min averages at intervals of 20 min. All instruments resolved 1-m vertical cells. The instrument at #A0 is still operational, and data can be accessed at http://simcosta. furg.br. Unfortunately, technical problems with the ADCP at #A1 caused a data gap between December 12 and February 28. Data from #A0 between 2014 and 2016 was extensively analyzed by Thévenin et al. (2019). Among the data measured at A0, only the temperature time series will be used in this study. Supplementary hydrographic data on April 08, 2013, was obtained with vertical CTD profiles at stations I–IV (Fig. 1) using a SeaBird 19-Plus instrument.

The available current data had its upper five depth cells removed (first 5 m of the water column) in several data segments, a protocol commonly used with ADCP records to avoid the noise produced by the side-lobe effect. Only a few raw files were obtained for the 2014 deployments, and a complete representation of the vertical velocity profiles is thus limited to the beginning of the time series (Nov 2014–Jan 2015).

Daily sea-surface temperature (SST) for an area of the continental shelf fronting the BTS (polygon in Fig. 1) was obtained from the *Multi-scale Ultra-high Resolution* (MUR, https://podaac-opendap.jpl.nasa.gov/opendap/allData/ghrsst/data/GDS2/L4/GLOB/JPL/MUR/v4.1/) platform, with a spatial resolution of 800 m. This polygon is coincident with the area defined by Santos et al. (2014) as a surface upwelling hotspot. Daily-mean Paraguaçu River (Fig. 1) discharge was provided by Votorantim Energia, the energy concessionary managing Pedra do Cavalo dam (see location in Fig. 1).

Supra-inertial and tidal frequencies were removed from the time series by applying a Lanczos spectral filter with a cutoff frequency of 53 h, which is the inertial period at this latitude. The shear intensity of the subtidal flow aligned with he channels axis, a proxy for the intensity of the gravitational circulation, was calculated by the difference between the subtidal flow velocity between 2 m and 4 m above the bottom and the subtidal flow velocity between 4 m and 7 m below the surface (only when surface data existed). The more surficial velocity cells were disregarded because of the wind influence (surfacial wind boundary layer).

The upwelling events were identified by negative trends of the sub-inertial temperature oscillations of at least 0.2 °C·day^{-1} for more than 2 days (Tapia et al. 2009), beginning when the temperature starts to decrease and ending at the minimum temperature. This is different from the negative temperature anomaly (e.g., Benazzouz et al. 2014) or thermal signature (e.g., Palóczy et al. 2014) approach, which tends to identify only the climax of the
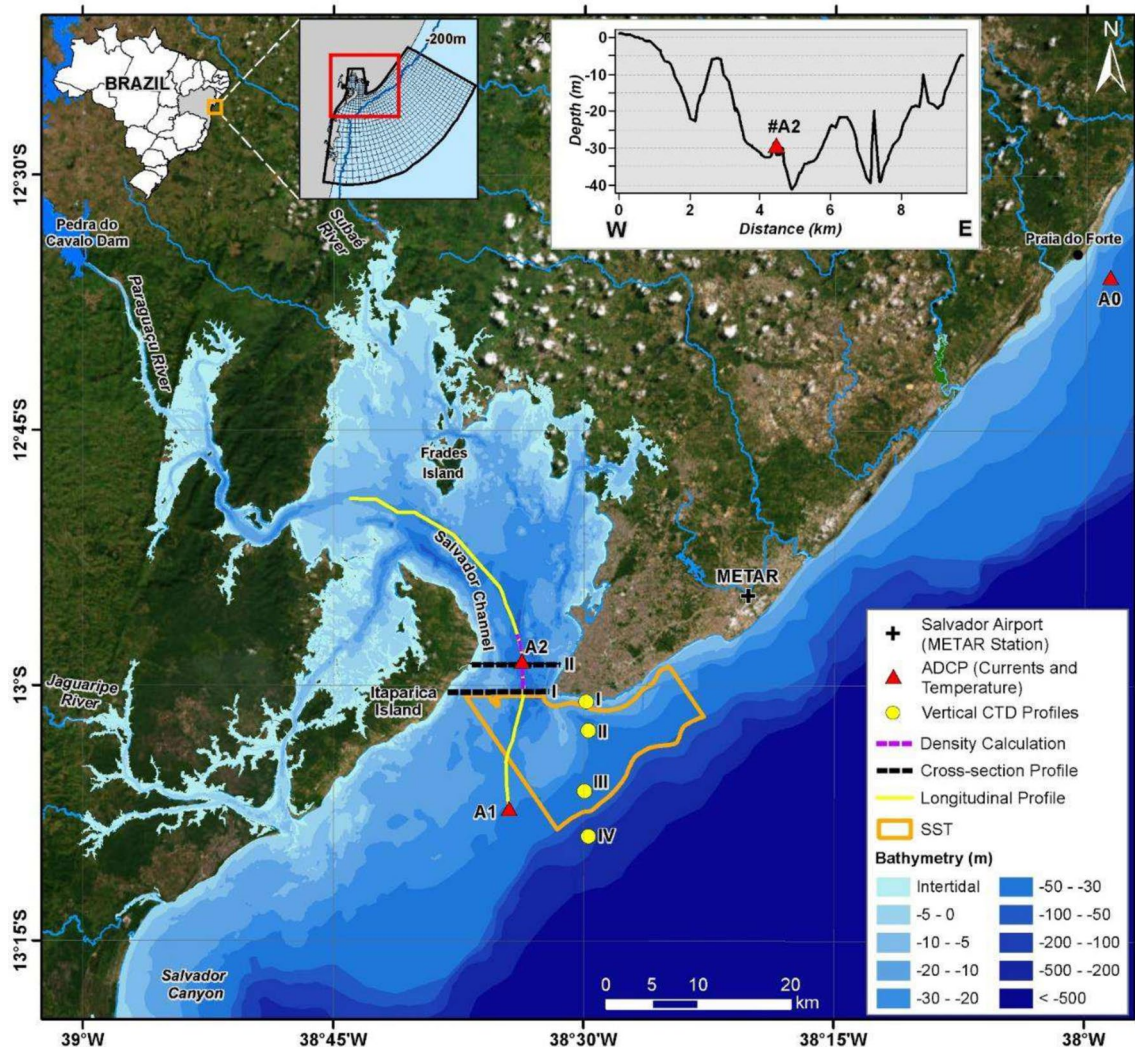
Fig. 1 Location of Baía de Todos os Santos Bay with the domain of the numerical model, bathymetric contour, moored ADCP stations, and the perimeter (in orange) of the shelf area where the daily mean SST was calculated. The yellow line indicates the path of the longitudinal hydrographic transect discussed in the text. The pink dashed segment on the yellow line indicates the distance (14 km) where density gradients most influence the gravitational circulation. Dashed black lines are related to the bathymetric transect shown in the inset (II), and to Aguiar et al. (2019) cross-sections (I) discussed in the text

process near its closure, even including a period of increasing temperatures after the upwelling process has ceased.

Data on wind velocity and direction was obtained from a METAR station (SBSV) at the Salvador International Airport (Fig. 1). The wind vectors were rotated 180° (oceanographic reference frame), aligned with the coast and decomposed into alongshore (v) and cross-shore (u) wind components. The METAR station is located 6 m above the ground, 1.5 km inland from the shoreline, and 29 km to the NE of the bay entrance. Data is acquired hourly. The effects of the sea and land breezes were removed by applying a Lanczos loss-pass spectral filter with a cutoff period of 53 h.

Numerical Model

We used numerical model results from a simulation for the years 2008–2014 (Marta-Almeida et al. 2019) using the Regional Ocean Modelling System (ROMS; Shchepetkin and McWilliams 2005). In this investigation we selected hourly model results between January 2012 and December 2014.

The model domain (Fig. 1, inset) included the bay and the continental margin between the latitudes 14.4°S and 12.25°S. The horizontal model resolution varied between 1200 m offshore and 300 m inside the bay. The vertical discretization used 32 terrain-following levels. The grid

bathymetry was obtained from a blend of ETOPO (Amante and Eakins 2009) and very high-resolution (up to 1:8000) nautical charts produced by the Brazilian Navy. The shallowest depth of the digital terrain model was 5 m, meaning that emersion and submersion of intertidal areas were not reproduced by the model.

The surface atmospheric forcing was obtained from the Climate Forecast System Reanalysis (CFSR; Saha et al. 2010). The model used the atmospheric variables — wind, temperature, pressure, precipitation, humidity, net shortwave radiation, and downward longwave radiation — to calculate the surface fluxes via bulk formulae. Tides were imposed at the model open boundary through the main harmonic components (M2, S2, N2, K2, K1, O1, P1, Q1) from TPXO 7.1 (Egbert and Erofeeva 2002). Lateral forcing was obtained from the Hybrid Coordinate Ocean Model in conjunction with the Navy Coupled Ocean Data Assimilation (HYCOM/NCODA, HYCOM, 2011) as daily values having horizontal resolution of 1/12°.

The riverine sources of the bay were incorporated in the modelling configuration using measured and estimated discharges for the three main rivers (Paraguaçu, Subaé, and Jaguaripe; Fig. 1) as well as the peripheral tributaries, which were distributed in eight locations around the bay.

The modelling configuration ran offline nested in a larger high-resolution domain (horizontal resolution of 1/36°, described in Amorim et al. 2013). This parent configuration was initiated and forced at the boundaries by solutions of the global model HYCOM–NCODA, with horizontal resolution of 1/12 (Wallcraft et al. 2009). For a full description of the present configuration, see Marta-Almeida et al. (2019). The results of this model run were also used by Marta-Almeida et al. (2017), who investigated the BTS tidal potential energy; Aguiar et al. (2018), who studied the upwelling processes along the BTS adjacent shelf and inside the Salvador Canyon; Aguiar et al. (2019), who analyzed the bay-shelf exchange dynamics; and Mariani et al. (2021) who investigated long-term salinity trend of the bay.

To assess the importance of the wind stress and both the horizontal and vertical density differences on the establishment of the subtidal flow, we used three dimensionless ratios, namely Wedderburn (Wn), Simpson (Si), and Bulk Richardson number (RiB), calculated with daily means outputs from numerical models. The Wedderburn number considers the effects of the wind stress and the horizontal density gradient, and is given by

$$W_n = \frac{\tau_{wv} L}{\delta \rho_x \, g \, H^2}$$

where L is estuary fetch length (30 km straight section longitudinal to the entrance channel), ρ_x is the horizontal density gradient along the same distance, g is gravity, and H is the mean water depth. The wind stress longitudinal to the channel axis ($\tau_w v$) was calculated following the equation proposed by Trenberth et al. (1989), where $\tau_{wv} = \rho_a \, C_{dw} \, |U_v||U_v|$, with the air density ($\rho_a$) equal to 1.2 kg·m^{-3}. The wind velocities from CFSR are representative of the center of the bay. The wind drag coefficient (C_{dw}) was assessed through the polynomial best fit to the distribution of Edson et al. (2013) averaged drag coefficients vs 10-m-high ocean wind speed. For $W_n > 1$, the wind stress prevails over the baroclinic pressure gradient force on the entrainment of surface waters.

The Simpson number indicates whether horizontal density gradients driving tidal straining can overcome the mixing effect of turbulence induced by the bottom drag, and is given by

$$S_i = \frac{g \, \delta \rho_x H}{C_d \, U^2}$$

where C_d is the drag coefficient (commonly 0.0025) and U the vertically averaged tidal velocity amplitude. Becherer et al. (2011) indicate an S_i threshold of 8.8×10^{-2} between well-mixed (unidirectional vertical-mean speeds) and periodically stratified flows (episodic strain-induced sheared subtidal flows), and an upper threshold of 8.4×10^{-1} for permanently stratified flows. The bulk Richardson number relates the stabilizing effects of the vertical density differences and the mixing capacity of the current shear

$$R_{iB} = \frac{g \, \Delta \rho H}{\rho_o \, U^2}$$

where $\Delta \rho$ is the density difference between the bottom and surface and ρ_o is the reference density (1024 kg·m^{-3}).

Study Area

The BTS (12°50′ S and 38°38' W) is a large (1223 km^2) tectonic, well-mixed, positive estuary (Cirano and Lessa 2007) situated behind the narrowest (10 to 15 km wide) stretch of the western South Atlantic shelf (Castro and Miranda 1998). The bay has maximum and average depths of 60 m and 9.6 m, respectively, with a main northern inlet (Salvador Channel, Fig. 1) 10 km wide and 30 m deep, on average.

The local tides are semi-diurnal, with Form Number (F = K_1 + O_1/M_2 + S_2, Defant 1961) varying from 0.11 on the shelf to 0.06 inside the bay, and explain 97.5% of sea-level variability. The tidal range on the shelf is amplified 1.5 times along the bay, with the main lunar semi-diurnal component (M_2) growing from 0.67 m to 1.06 m 60 km upstream (Cirano and Lessa 2007). Maximum tidal current magnitude in Salvador Channel is larger than 1.0 m·s^{-1} (Marta-Almeida et al. 2017), with stronger ebb flows. The subtidal flow along the
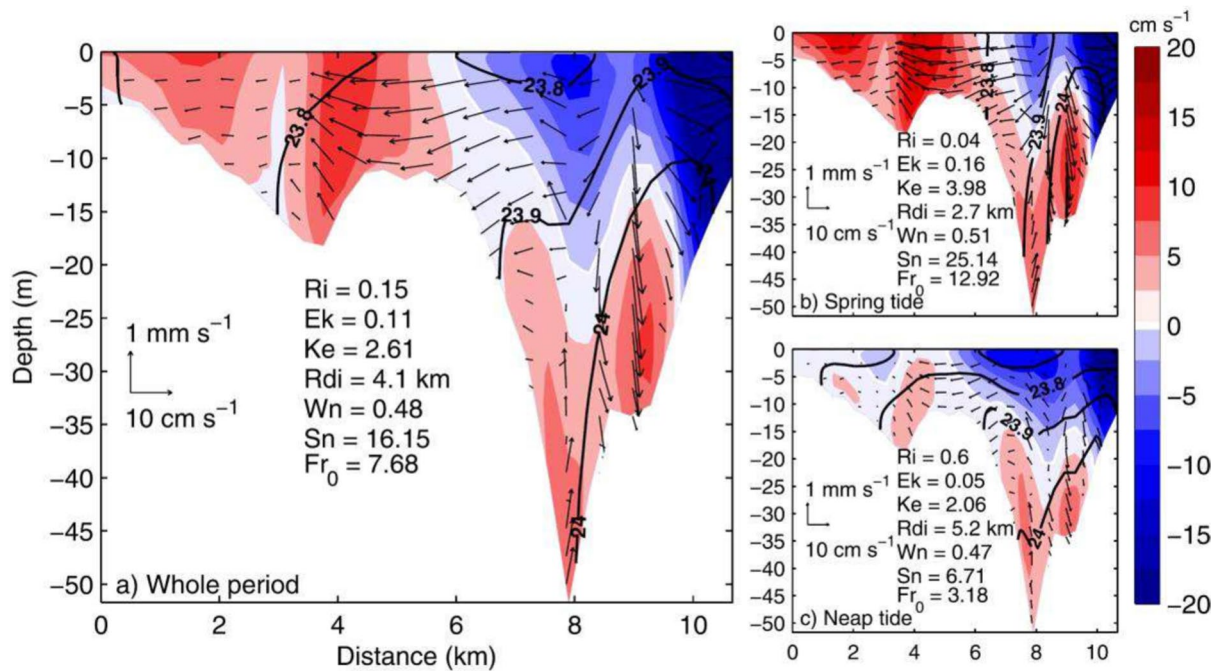
Fig. 2 Characteristic axial (colors) and normal (vectors) flow structure in a E-W cross-section profile at the bay mouth (see Fig. 1 for location). Results are 7-year averages from numerical simulation. Black lines are isopycnal contours. Positive axial flow values denote inflow. Dimensionless numbers listed are as follows: Richardson (Ri), Ekman (Ek), Kelvin (Ke), Wedderburn (Wn), stress ratio (Sn), and Froude (Fr$_o$). Rdi is the Rosby radius. From Aguiar et al. (2019)

main channel is sheared and modulated by the spring-to-neap tidal cycle, with maximum subtidal flow speeds during neap tides in the order of 0.25 m·s^{-1} (Lessa et al. 2018). Across Salvador Channel, the flow is vertically sheared during neap tides, and both horizontally and vertically sheared during spring tides (Fig. 2) (Aguiar et al. 2019). The wind intensifies the estuarine bi-directional exchange at the mouth during the spring and summer, and eventually reverses the longitudinal flow structure when blowing from the south in the autumn and winter. Aguiar et al. (2019) investigated the balance of the forces and their effects on the subtidal circulation at the bay mouth (see their cross-section location in Fig. 1) using several dimensionless numbers, namely Wedderburn (Wn), Ekman (Ke), Kelvin (Ke), stress ratio (So), tidal Froude (Fr$_o$), and Richardson (Ri) numbers. Their results showed (Fig. 2) that the mean exchange flow at this 19 km wide cross-section is always stratified during neap tides (Ri = 0.6) and more influenced by rotational than frictional effects (Ek = 0.11 and Ke = 2.61), causing a more horizontally than vertically sheared flow. Tidal rectification dominates over gravitational circulation (Fr$_o$ > 1), which, in turn, dominates over wind stress (So > 1). Baroclinicity prevails most of the time (Wn < 1).

Seasonally, river discharges, mainly from Paraguaçu River (Fig. 1), also regulate the subtidal flow. While the Paraguaçu River flow is highest in the summer, the discharge from small peripheral tributaries is maximum between April and July (Aguiar et al. 2019; Santana et al. 2018). The Paraguaçu River discharge is regulated by Pedra do Cavalo dam (Fig. 1), which since 1986 has reduced the freshwater yield to BTS by 62% of its climatological mean discharge of 66.7 m^3·s^{-1} (Mariani et al. 2021). Given the relatively very small freshwater discharge (< 0.1% of the tidal prism), higher density gradients are restricted to the most internal part of the bay. The mean density gradient along the main channel (~ 50 km long) grows from 0.042 kg·m^3·km^{-1} in Salvador Channel to 0.095 kg·m^3·km^{-1} close to Paraguaçu River mouth (Lessa et al. 2019).

Wind-driven coastal upwelling events are frequent between September and March, and longer lasting and more intense in front of the BTS (Santos et al. 2014; Thévenin et al. 2019). The upwelled water is advected from depths between 80 and 100 m, and about 60% of the shelf-break upwelling events reach the surface (Thévenin et al. 2019). The upwelling events last between 4 and 21 days, which in turn cause temperature drops of up to 4.2 °C and negative thermal anomalies as high as − 2.8 °C (Thévenin et al. 2019). Besides the chief role of wind, cyclonic eddies were also shown to be important in driving upwelling events (Thévenin et al. 2019). Additionally, Salvador Canyon, situated 40 km southwest from the BTS (Fig. 1), locally

elevates the isotherms when the contour current hugs against the slope, also facilitating upwelling events in front of the BTS (Aguiar et al. 2018).

Results

In this section, we will address data acquired between November 2014 and January 2015 using observed and modeled data. Additionally, we will present results from the numerical simulations for the summer/autumn of 2013, when the upwelling was critical to reestablish the estuarine longitudinal density gradient.

Observed Data and Numerical Model Results for 2014/2015

The variations of tide range, Paraguaçu river-dam outflow, bottom water temperature, and the vertical structure of the flow longitudinal to the channel axis at stations #A1 and #A2 between November 2014 and October 2015 are shown in Fig. 3. The data displays a clear seasonal cycle of the bottom water temperature (Fig. 3C), with a warming

phase between September and April that was more continuous in the SST field. The records of bottom temperatures were quite irregular due to several upwelling events that are almost synchronous at stations #A0 and #A1. The temperature increase at the bottom between September and March was lessened by a quasi-permanent vertical advection of colder water in the austral spring and summer (Thévenin et al. 2019), which established offsets of up to 2.4 °C between bottom and surface temperatures. Individual upwelling events were thus the eventual intensifications of the advective processes caused by the strengthening of southwestward wind speeds (negative shore-parallel speeds) and/or close proximity of cyclonic eddies. The lowest temperatures were 22.8 °C at #A0 in October 2015, followed by 24.3 °C at #A1 in November 2014.

Oscillations of the SST did not follow those at the bottom closely. The highest correlation coefficient (r) of 0.66 was obtained with no time lag between the time series. Correlation between bottom temperature records from #A1 and #A0 was 0.84 with a time lag of 24 h (#A1 leading #A0). Close to 62% of the upwelling events recorded at #A1 and #A2 occurred during neap tides.
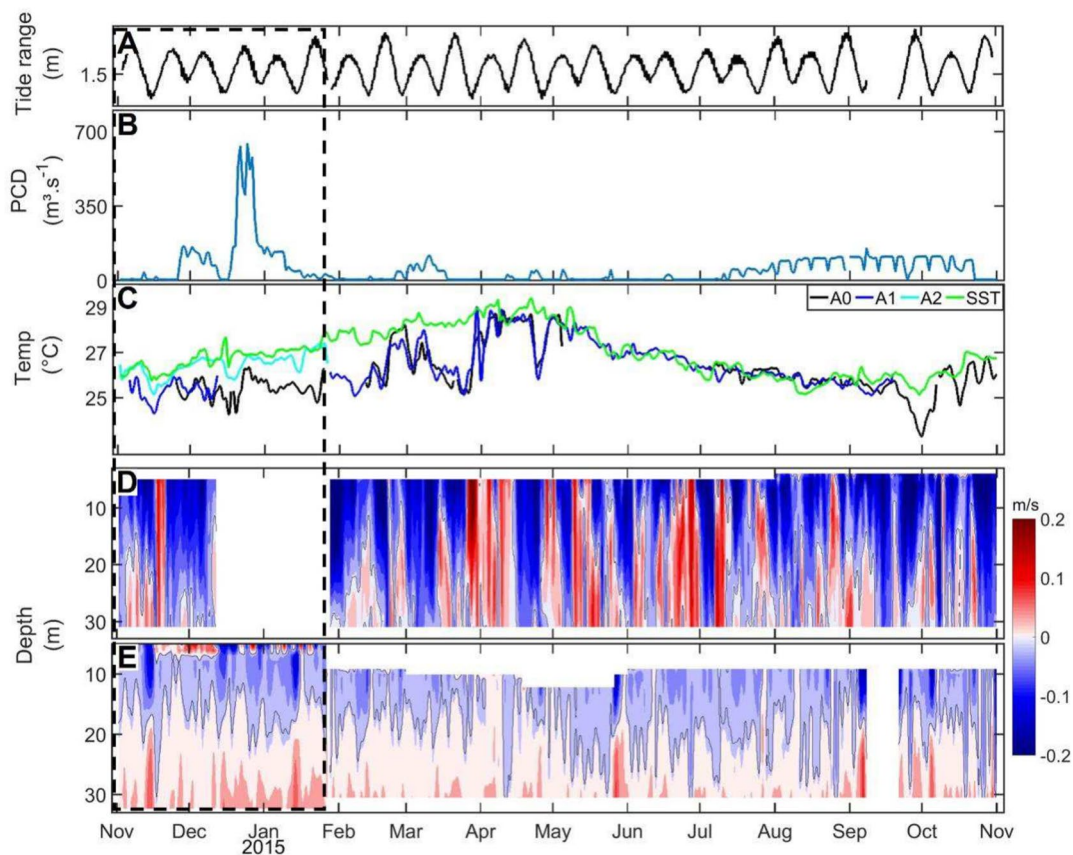

Fig. 3 Variability of observed tidal ranges at #A2 (**A**), daily-mean Paraguaçu River dam discharge (**B**), low-pass filtered (53 h cutoff) water temperature at the bottom of #A0, #A1, #A2 and on the surface—SST (**C**), vertical profiles of subtidal flow speeds at #A1 (**D**) and #A2 (**E**). The dashed rectangle highlights the data section shown in Fig. 4

Higher Paraguaçu River dam discharge (Fig. 3B) occurred in December 2014, with a maximum daily mean discharge of 644 m³·s⁻¹. The mean dam discharge for the 12 months was 95 m³·s⁻¹, and very small discharges were observed between March and July.

The subtidal flow at #A1 (Fig. 3D) was mostly sheared between November and December 2014, and between August and October 2015. Vertically unidirectional flows, with alternating directions, was observed between April and July. At #A2 (Fig. 3E), the subtidal flow was vertically sheared throughout the time, although with speeds lower than at #A1. More intense vertical shear occurred between November and January, and in September and October (as indicated by bottom speeds). The highest shear occurred during neap tides.

A more detailed analysis of the hydrographic conditions is performed below for the period between November 2014 and January 2015 (dashed rectangle in Fig. 3).

Conditions in the Summer 2014–2015

A summary of the overall hydrographic conditions at #A1 and #A2 between November 2014 and January 2015 is presented in Fig. 4. During this time period, five spring-neap tidal cycles were observed (Fig. 4A), with three neap phases (Nov 14th, Dec 15th, Jan 15th) having ranges smaller than 1 m. The vertical structure of the subtidal flow at #A1 (Fig. 4B) alternates between sheared and non-sheared, with maximum speeds of 0.2 m·s⁻¹. Sheared flows attained maximum shear intensity of 0.25 m·s⁻¹ in November (Fig. 4D), concurrent with an upwelling event (Fig. 4C) associated with a temperature decrease of 0.27 °C and minimum temperature of 24.3 °C on November 16, coincident with neap tides. The upwelling event started on November 9, with cooling rates of 0.5 °C·day⁻¹, 15 h after the beginning of a long-term rise in the shear intensity (gray lines in Fig. 4C, D). The upwelling then ceased 24 h after the shear
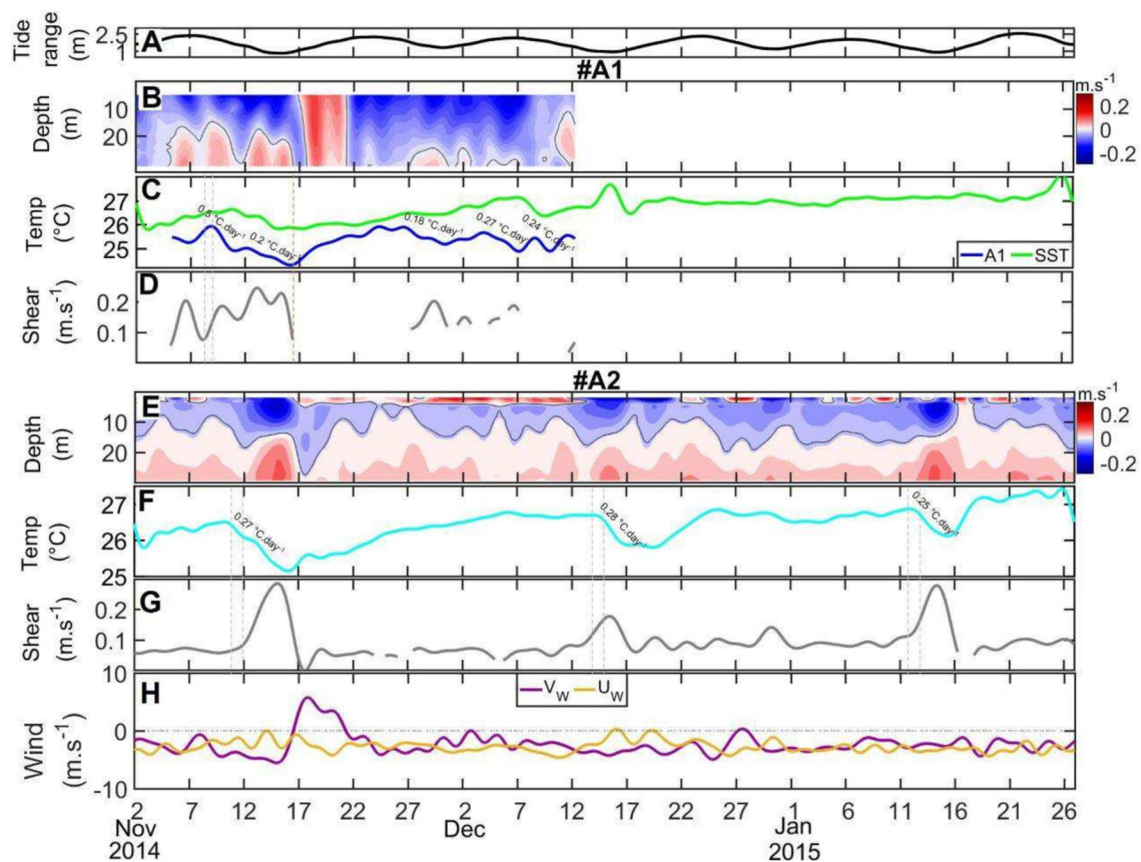

Fig. 4 Time series of observational data at #A1 and #A2 between November 2014 and January 2015. **A** is the tidal range for every tidal cycle measured at station #A2. **B** and **E** are vertical profiles of subtidal flows at #A1 (shelf) and #A2 (Salvador Channel), respectively. **C** and **F** show the variation of the bottom temperature (lines) and cooling rates (numbers) at #A1 and #A2, respectively. **D** and **G** show the velocity shear intensity at #A1 and #A2. **H** is the subinertial alongshore and cross-shore wind speed from Salvador International Airport. Vertical gray lines mark the time for the onset of the upwelling event and velocity shear intensification

intensity started its last decline (orange line Fig. 4C, D). The water temperature increased 1.6 °C through the next 10 days when flow shear was absent. The unidirectional flows during this period alternated between landward and seaward, with the former associated with an event of positive alongshore winds, and strengthening of the negative cross-shore wind, that lasted for 4 days (Fig. 4H).

Still at station #A1, the water cooled again on November 27 in the following neap cycle when flow shear was once more established. This cooling was, however, not fast enough to be classified as an upwelling event (cooling rate of 0.18 °C·day^{-1}). Once more, the beginning and end of this cooling event followed the beginning and end of a short-lived shear episode.

At station #A2 the subtidal flow was permanently sheared, very often with three layers when along-channel winds forced upstream (positive) flows in the upper 4 m of the water column (a surface boundary layer, Fig. 4E). The subtidal flow speeds and shear intensity increased in all but one of the neap tides (November 30). Three upwelling events were observed in the time series: on November 10 (concurrent with the event at #A1), on December 14, and on January 12 (Fig. 4F). The first event was the coldest and longer-lasting, with a continuous temperature decrease for 6 days and minimum temperature of 25.1 °C. The lowest temperature was recorded 1 day after the maximum shear intensity (Fig. 4G). The temperature fell 12 h after the upwelling event began at #A1, and preceded by 1 day the local increase in the velocity shear (gray lines in Fig. 4F, G). The coldest temperature, 0.69 °C warmer than at #A1, indicating the end of the event, was preceded by a decrease in shear intensity.

The second upwelling event on December 14 resulted in 3 days of fast temperature decrease at #A2 (0.28 °C·day^{-1}), and was followed by 1 more day of a slow temperature fall when two lows (25.9 °C and 25.8 °C) occurred 1 and 4 days after the maximum shear intensity. This second event was associated with the lowest shear intensity amongst the three events. The velocity shear started 24 h prior to the beginning of the cooling event (gray lines in Fig. 4F, G).

The upwelling event on January 12 initiated 24 h after an increase in flow shear, lasted for about 3 days and caused a minimum temperature of 26.1 °C, which occurred 20 h after the maximum velocity shear. The temperature increased again as the flow shear disappeared.

The numerical simulations properly reproduced the temperature variation, longitudinal current structure, and the shear intensity at #A2 (Fig. 5). The upwelling events that ended on November 16 and on December 20 are well replicated (Fig. 5B), as well as the concurrent acceleration of the gravitational circulation (Fig. 5E) and enhanced shear intensities (Fig. 5H). The alongshore component of the wind velocity was also properly replicated by the CFSR reanalysis (Fig. 5C). Vertical (Fig. 5F) and longitudinal

(Fig. 5I) density gradients are maximum mid-way through the upwelling event, simultaneous with maximum shear intensity, and start decreasing before the event is over. The shear intensity decreases while the temperature is still falling, coinciding with a reduction of the longitudinal density gradient. Density gradients were calculated for distances varying between 2.2 km and 30 km centered at #A2 (red dashed line in Fig. 1). Correlation coefficients between the time series of shear intensity and density gradients varied between 0.73 (2.2 km) and 0.3 (30 km).

The bulk Richardson number (Fig. 5G) indicates that the flow was always stratified during neap tides ($Ri_b > 0.25$), in agreement with Simpson's number higher than 8.8×10^{-1} indicating a permanently stratified flow during the upwelling events. The Wedderburn number (Fig. 5G) repeatedly smaller than 1 indicates that baroclinicity prevailed upon the wind shear in the bay. Only between Nov 17 and 22 the wind stress overcame the longitudinal density gradient ($Wn > 1$).

The Critical Role of Upwelling in Re-establishing the Estuarine Circulation in 2013

Using the results of the numerical model, we will investigate the dynamic scenario associated with the extreme draught in the summer of 2013, the driest in the historical record dating back to 1960. Hypersalinity (salinity higher than that on the shelf) in the bay was recorded with field data between December 2012 and April 2013 (Lessa et al. 2019). The results from the numerical model (Fig. 6) show that salinity starts to increase around December 17, 2012 (Fig. 6B), but with the maintenance of an estuarine density gradient (Fig. 6C) due to a concurrent increase in the bay's temperature (Fig. 6A). A reversal of the density gradient occurs 3 months later, around March 20. At this time, the bay's temperature was stable, but the temperature on the shelf still increased. The water density inside the bay thus became higher than that on the shelf, and the flow shear turned negative, i.e., an inverse estuarine circulation was established (Fig. 6E). This overturned density gradient was intensified on April 26 with a sharp decrease of the water temperature inside the bay. Although the salinity inside the bay lowered simultaneously (from 38 to 37.8), the water density increased (Fig. 6C). A faster salinity reduction in the last few kilometers of the longitudinal profile ended up creating a conspicuously localized density maximum (density plug) between April 26 and May 6 some 40 km inside the estuary (Fig. 6C). The density plug disappeared by mid-May with the onset of a belated rainy period (Lessa et al. 2019).

The modeled subtidal flow at #A2 was regularly sheared (Fig. 6D, E) until March 20, when the density on the shelf decreased and the longitudinal density gradient became minimal. After a period of 35 h of weak negative estuarine gravitational circulation (negative shear intensities on March 20th

Fig. 5 Time series of observational and modeled data at #A2 between November and December 2014. **A** observed tidal ranges, **B** observed and simulated bottom water temperatures, **C** low-pass filtered alongshore wind velocity component from observations and CFSR reanalysis, **D** observed vertical profiles of subtidal flows, **E** the same for model results, **F** vertical density profiles, **G** calculated Simpson (Si), Bulk Richardson (Ri$_b$), and Wedderburn (Wn), numbers (**H**) observed and simulated velocity shear intensities, and (**I**) longitudinal density gradients associated with a distance of 2.2 km centered at #A2
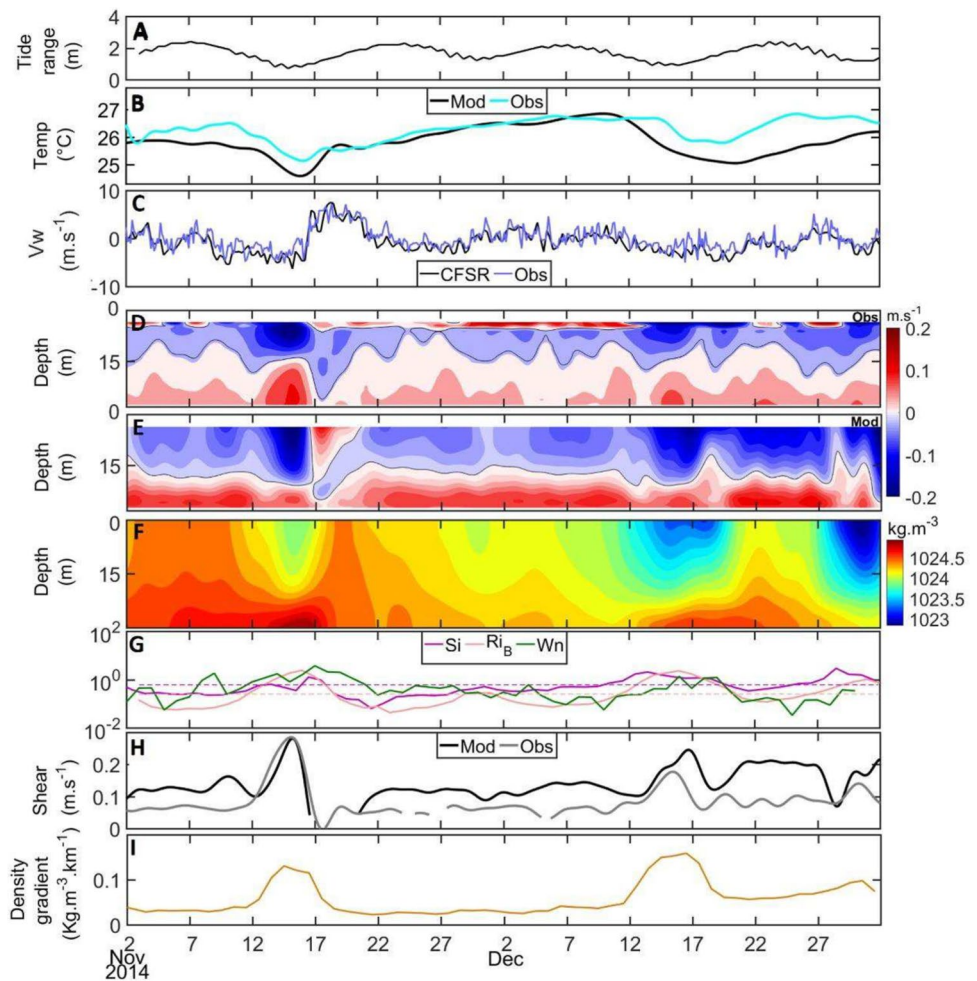
in Fig. 6E), flood-oriented, unidirectional subtidal flows prevailed, with faster speeds close to the bottom. Regular estuarine gravitational circulation was momentarily re-established around April 15 (Fig. 6D, E) as a result of a weak upwelling event (cooling rate of 0.1 °C·day^{-1}, Fig. 6A), and increasing water density (Fig. 6C) on the shelf 2 days earlier. Figure 7 documents, with data from CTD vertical profiles, the initial stages of this upwelling event on the shelf on April 08, when waters 2.2 °C cooler than those at surface occupied the shelf and increased the water density by 0.8 kg·m^{-3}. In the remaining period with the density plug well established, unidirectional, flood-oriented sub-tidal flows prevailed at station #A2, but now with higher speeds closer to the surface. Figure 8 presents the net flow across a transect normal to the channel intersecting station A2 for (a) the entire simulation period between 2008 and 2014, and (b) between April 26 and May 6, when the density plug was well established. The net flow for the 8 years of simulations shows both horizontal and vertical flow stratifications, somehow similar to the residual profile of Aguiar et al. (2019) at the bay entrance (Fig. 1). It is observed, however, that the flow was mostly horizontally stratified during the density plug period, but

with a narrow section to the right of station #A2 showing inverse estuarine circulation. This inverse flow structure might have been strengthened after April 17th, when the plug was at its maximum. Therefore, the inflow close to the bottom must have been decelerated given the existence of opposing pressure gradients in the nearby area, causing the lower speeds close to the bottom (Fig. 6D). Additionally, the onset of south winds blowing into the bay (positive alongshore winds, Fig. 6F) caused stronger inflow closer to the surface, as shown by well-correlated oscillations of the alongshore wind speeds and surface subtidal flow velocities.

Discussion

The vertically sheared estuarine circulation is observed across the narrow continental shelf fronting the BTS, where the flow shear intensity undergoes similar oscillations to those observed in the entrance channel (Fig. 4) and where the mean speed of the (non-filtered) cross-shelf flow is 1.4 times stronger than the along-shelf flow. The mean subtidal flow shear at #A1 (Fig. 3D) between November and March
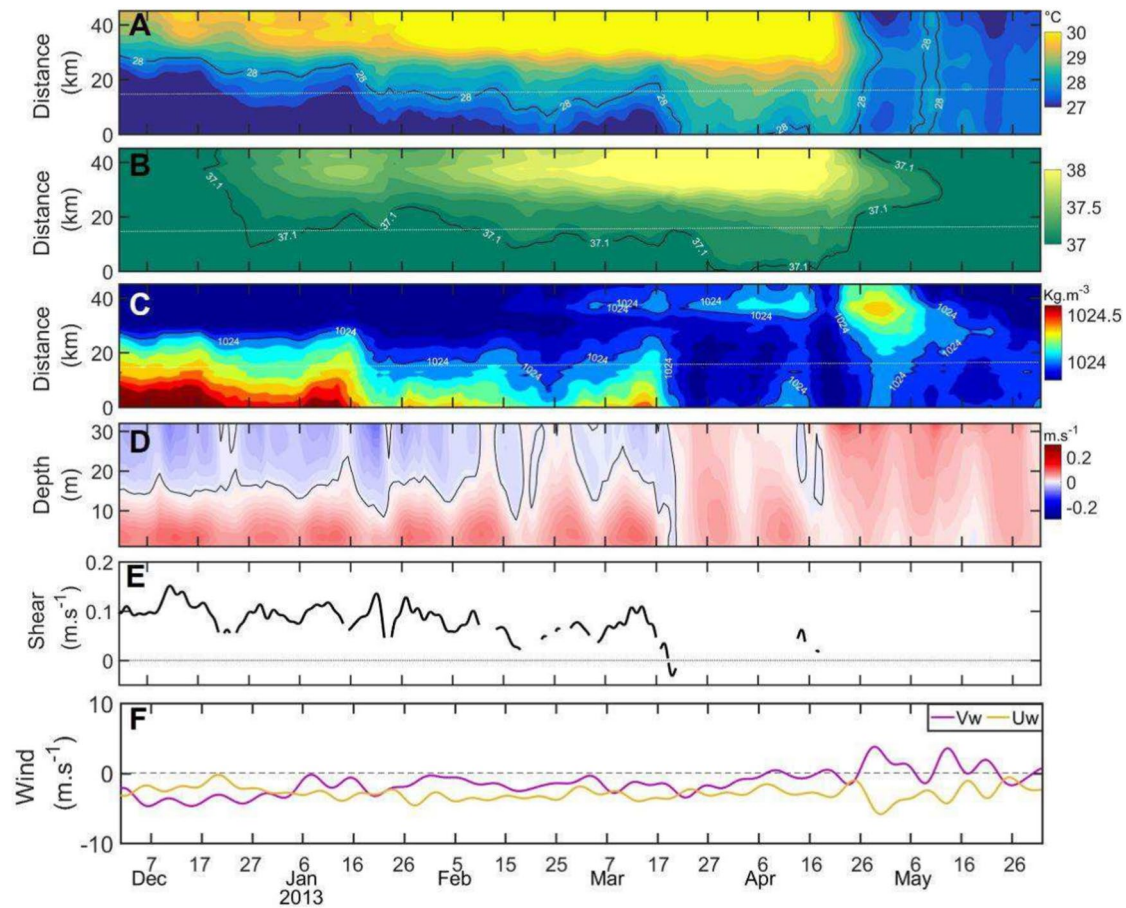
Fig. 6 Time and space variability of the simulated longitudinal profiles (see location in Fig. 1) of vertically mean temperature (**A**), salinity (**B**), and density (**C**) between December 2012 and May 2013. Vertical structure of the along-channel subtidal flow simulated at station #A2 (**D**), with outflow in blue and inflow in red, the alongshore (V_w) and cross-shore (U_w) components of the wind (**E**), and the corresponding shear intensity (**F**) in the same time period. Horizontal dashed lines in (**A**) to (**C**) indicate the position of #A2. Distances in **A** to **C** start at #A1 (see station location in Fig. 1)

(0.13 m·s^{-1}) was 22% higher than the mean between April and September (0.11 m·s^{-1}), when the upwelling did not occur and there was almost zero vertical temperature differences. Stronger gravitational circulation around December, as also evident at #A2 (Fig. 3E), is apparently ascribed to both higher water temperatures inside the bay and simultaneous cooling on the shelf, which increased the longitudinal density gradient. Although the increase in shear intensity also coincides with higher freshwater discharge from the Paraguaçu River dam, no significant correlation was found between these two variables, considering time lags between 5 h and 200 days.

Observed changes in temperature and longitudinal density gradients within the BTS, when under the influence of coastal upwelling, are similar to those mentioned at estuaries associated with strong upwelling systems of the east ocean margins. In Tomales Bay (California), Harcourt-Baldwin and Diedericks (2006) showed that density (temperature) gradients of approximately 0.2 kg·m^{-3}·km^{-1} (0.8 °C·km^{-1})

in a 5-km-long transect are created in the summer, the low inflow season, by upwelled water. These gradients are similar to those observed in the BTS considering similar distances (Fig. 5I). In Ria de Vigo (Spain), Barton et al. (2015) showed that water temperature 10 km upstream from the mouth decreased by 2 °C to 4 °C about 1 day after upwelling was detected on the shelf, where the lowest temperature was 13 °C. In the BTS, a reduction of 3 °C in the subtidal temperature signal was observed at #A2 40 h after the upwelling started at #A1, 15 km downstream, with lowest temperature of 25.1 °C (Fig. 4C, F). Lessa et al. (2019) report maximum temperature differences between shelf and bay waters of up to 4.6 °C in the summer.

The mean cooling rate associated with the upwelling events between 2014 and 2015 was 0.5 °C·day^{-1} at #A1 (Fig. 4), similar to those reported by Tapia et al. (2009) at 25 sites on the Chilean coast, where lowest temperatures reach 10 °C. These similarities between the upwelling recorded in our study region and at well-known upwelling systems
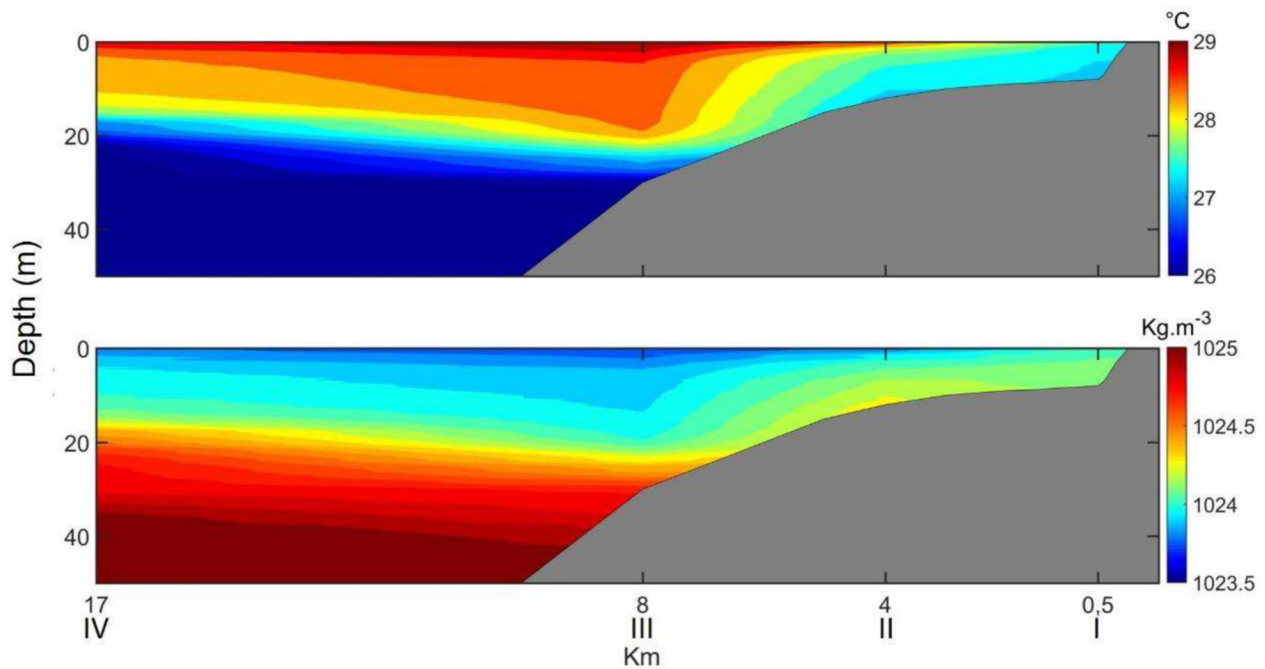
Fig. 7 Cross-shelf profiles of observed water temperature (**upper panel**) and density (**lower panel**) on April 08, 2013, showing cooler and denser upwelled water occupying the shelf near the entrance of the BTS

can be explained by upwelling processes of comparable strengths, with similar values for Ekman pump and transport (between 1 and 4 $m^2 \cdot s^{-1}$, Kämpf and Chapman 2016; Thévenin et al. 2019), and water being advected from similar depths (around 80 m).

Higher longitudinal temperature gradients created by colder water in front of the estuary generate larger baroclinic pressure gradients and acceleration of the gravitational circulation, as previously shown by Hickey et al. (2002), Giddings and MacCready (2017), and Harcourt-Baldwin and Diedericks (2006) in estuaries on the U.S. West Coast. The intensity of the gravitational circulation is also modulated by spring-neap cycles; it is accentuated during neap tides

when tidal-current residuals are minor, vertical mixing is weaker, and buoyance forces are stronger (Fig. 5G), favoring greater vertical segregation between denser incoming and lighter outgoing water masses. This fortnight modulation was pronounced in the BTS, where all three upwelling events investigated in detail were associated with neap tides (Fig. 4). Besides, 60% of all upwelling events recorded at #A1 between November 2014 and October 2015 were coincident with neap tides (Fig. 3A, C).

Different from previous studies, it was observed that the flow shear increased prior to the decrease of the temperature in two (December and January; Fig. 4F, G) of the three observed upwelling events. This indicates that the estuarine
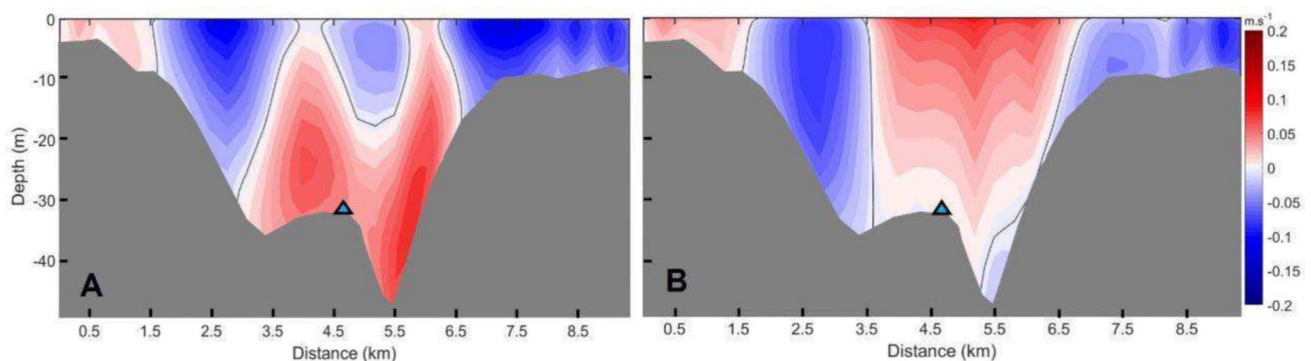

Fig. 8 Net along-channel flow from numerical model results at a cross-section coincident with station #A2. **A** Residual for all tidal cycles between 2008 and 2014. **B** Residuals between April 26 and May 6, during the strongest density plug. The triangle locates station #A2 mooring

gravitational flow can facilitate the upwelling event, possibly causing both its anticipation and local intensification. This is feasible because the estuarine circulation extends for more than 12 km out on the shelf (location of #A1), or at least 70% of the shelf width. This creates a suction mechanism similar to that described by Lü et al. (2006) on the shelf fronting the Yangtse River, where secondary cross-shelf circulation favors local upwelling. Surface upwelling in front of the BTS occurs more frequently and is colder than the surface upwelling at #A0 (Santos et al. 2014). This might be ascribed to more intense mixing, due to faster tidal flows, in front of the BTS, where mean current magnitude is almost twice as large than at #A0 (velocity data at #A0 is not shown).

Thévenin et al. (2019) showed that the wind is the main driver for coastal upwelling in the region, with cyclonic eddies playing a secondary role. It is interesting to notice that the wind was not always conducive to upwelling in

Fig. 10 Scheme of the progressive mechanism involved in an upwelling ▶ event fronting Baía de Todos os Santos during neap tides. Gray polygon represents a longitudinal topographic transect between the shelf break and the entrance channel, following the thalweg. Dashed black line at #A2 represents the elevation of the channel bottom at the station. Vertical gray dashed line indicates the bay entrance, and the topographic rise right before it is a section of an ebb-tidal delta. Blue shades represent varying water density (light shades smaller densities), the white dashed lines are isotherms, and the orange dashed lines are isopycnals (density in kg/m^3)

all three events here investigated. Figure 4H shows that negative (upwelling favorable) alongshore wind speeds occurred most of the time albeit with low speeds. Higher negative alongshore wind speeds were only observed preceding the first event. Because cyclonic eddies might have had some influence in those other two events, we used OSCAR (Ocean Surface Current Analysis) current data, with spatial resolution of 0.3°, between November 2014

Fig. 9 Distribution of the 5-day average ocean currents close to the BTS. Data from OSCAR (Ocean Surface Current Analysis), with spatial resolution of 0.3°
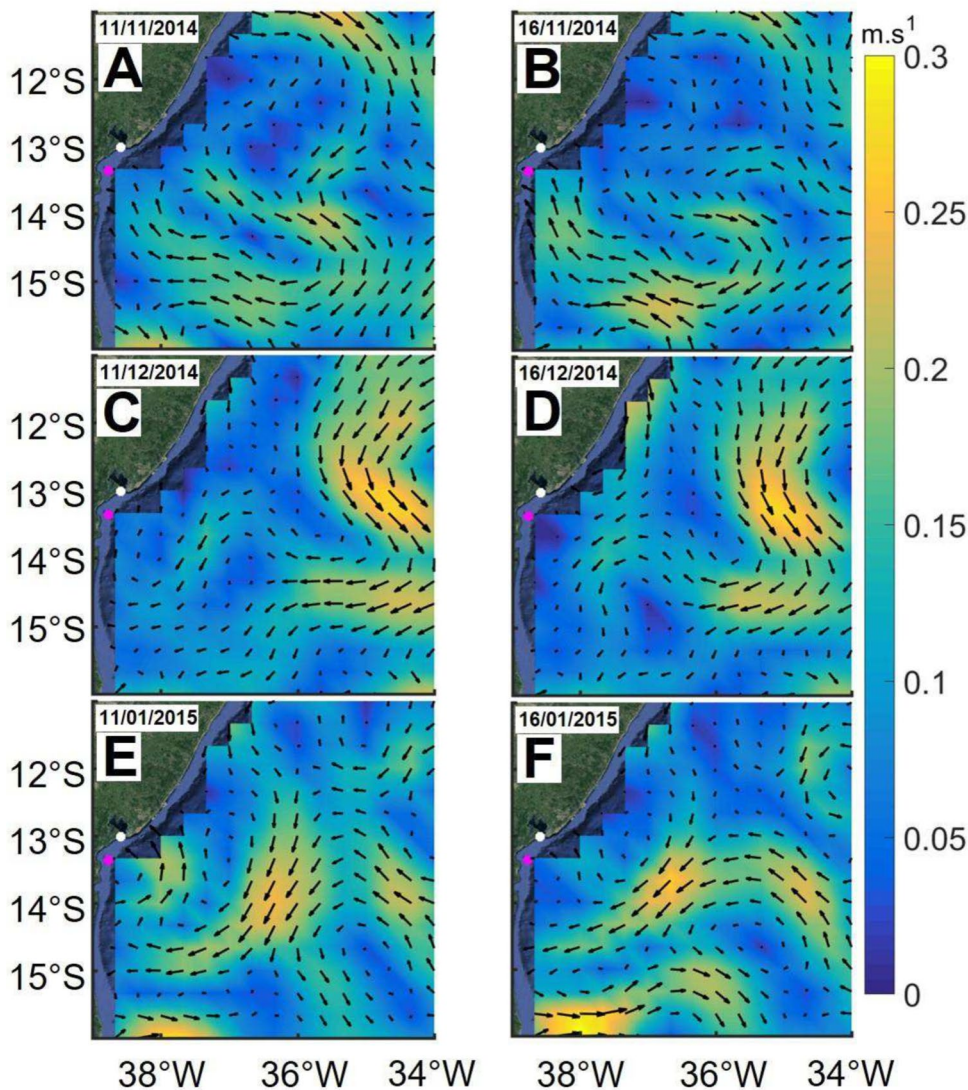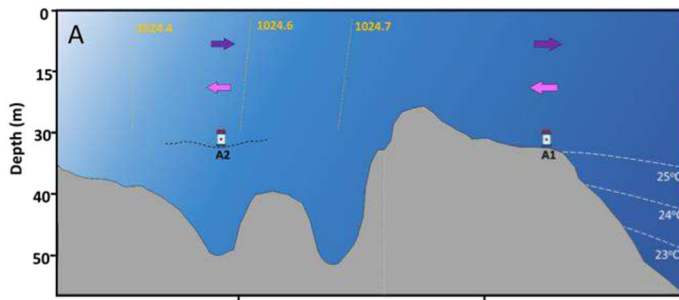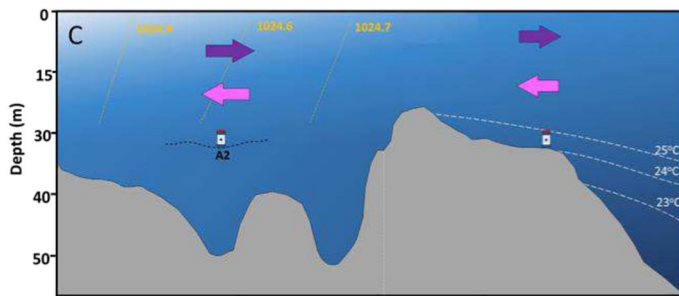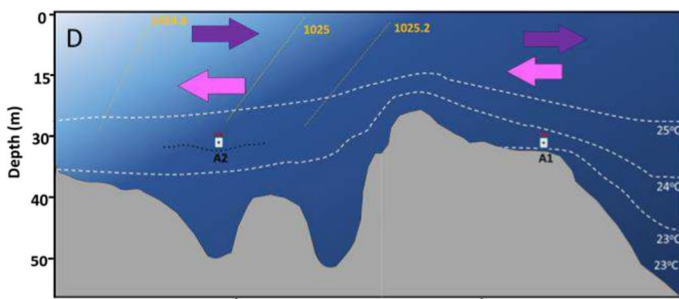
Weak estuarine gravitational circulation extends across the shelf. Small vertical/horizontal density gradients
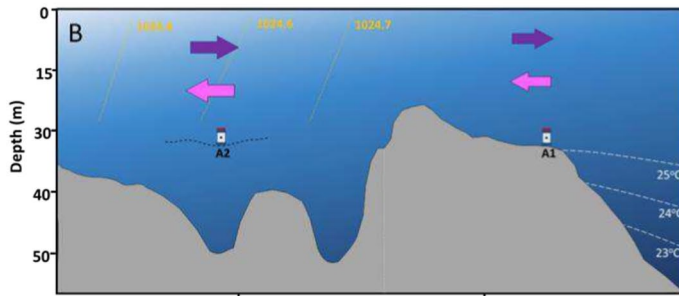
Strengthened estuarine gravitational circulation occurs during neap tides, with increasing vertical density gradients

Upwelling is initiated with colder creeping onto the shelf, density gradients increase first outside the bay

Upwelled water enter the estuary, density gradients increase and velocity shear is enlarged. As the heaviest water is advected through the thalweg, the shallower instrument position inside the estuary does not record the lowest temperatures.
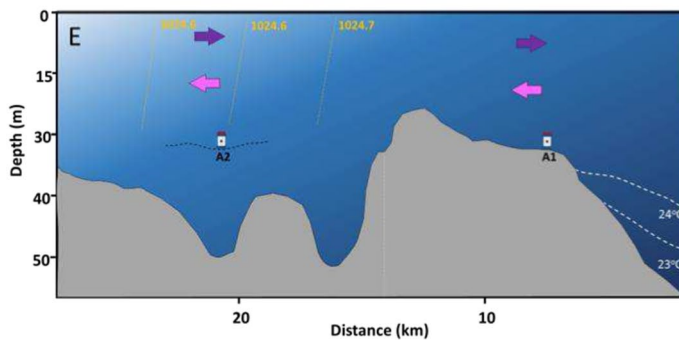
Past neap tides density gradients become smaller, velocity shear is reduced and upwelling ceases.

and January 2015, to look into the circulation on the nearby continental margin. The data is available at https://podaac-opendap.jpl.nasa.gov/opendap/allData/oscar/preview/L4/oscar_third_deg/. The spatial distributions of the current vectors (Fig. 9) show a cyclonic eddy close to the entrance of the BTS only in November (possibly on December 11), which might have worked as an accessory to the first upwelling event, which was the strongest and the longest one. Hence, because the participation of the most important upwelling drivers was either questionable or absent, the estuarine gravitational circulation gains importance as a driver for local upwelling, acting at least as a facilitator of the process.

Regardless whether gravitational circulation leads upwelling or vice versa, the whole process apparently engenders a cycle of initially positive and later negative feedback mechanisms. Figure 10 presents a graphical scheme of the mechanism considering that increasing gravitational circulation close to neap tides initiates the process. Weaker vertical mixing and increased current shear across the shelf (Fig. 10B) draw in slope water onto the shelf (Fig. 10C) that enlarges density gradients and boosts the gravitational circulation (Fig. 10D). This quickly advects water into the bay, reducing the temperature and the density gradients (Fig. 10E), which then slow down gravitational circulation even before the end of the upwelling event on the shelf. Subtidal circulation and the thermohaline structure then return to the initial stage.

Conclusions

Summer coastal upwelling causes substantial effects upon the subtidal circulation of Baía de Todos os Santos. Upwelling events cause positive density anomalies on the shelf that strengthen the longitudinal density gradients and intensify the gravitational circulation at the bay entrance. The advection of cold water into the bay eventually diminishes the longitudinal density gradient and decelerates the gravitational circulation before the upwelling event ceases. A return to a pre-event shear intensity coincides with the beginning of a warming trend in water temperature, closing a positive-negative feedback loop. Upwelling is also important to restore gravitational circulation when hypersalinity is established in the bay and density gradients fall to a minimum late in the summer.

Increasing speeds of the vertically sheared flow during neap tides tend to lead upwelling events. Given the regionally narrow continental margin, the estuarine gravitational circulation during these tidal phases is enhanced across the shelf and, as a suction mechanism, facilitate the upwelling process, boosting the upward advection of water from the slope, which will then further accelerate the gravitational circulation.

Because the regional climate has undergone a long-term trend of aridification, with declining precipitation and river discharges, and the bay has become hypersaline in the summers with severely depressed fluvial discharges, the strength of the gravitational circulation most likely has been reduced. In such a scenario, the role of upwelled water in maintaining the exchange flow increases, and might become especially important in the future given the predicted worsening of the regional draughts in the coming decades.

References

Aguiar, A.L., A. Valle-Levinson, M. Cirano, M. Marta-Almeida, G.C. Lessa, and J.F. Paniagua-Arroyave. 2019. Ocean-estuary exchange variability in a large tropical estuary. *Continental Shelf Research.* https://doi.org/10.1016/j.csr.2018.11.001.

Aguiar, A.L., Cirano, M., Marta-Almeida, M., Lessa, G.C., and Valle-Levinson, A. 2018. Upwelling processes along the South Equatorial Current bifurcation region and the Salvador Canyon (13°S), Brazil. *Continental Shelf Research.* https://doi.org/10.1016/j.csr.2018.10.001.

Amante, C., and Eakins, B.W. 2009. NOAA Technical Memorandum. *NESDIS NGDC-24 ETOPO1 1 Arc-Minute Global Relief Model: Procedures, Data Sources and Analysis.* https://www.ngdc.noaa.gov/mgg/global/relief/ETOPO1/docs/ETOPO1.pdf . Accessed 17 Jan 2023.

Amorim, F.N., M. Cirano, M. Marta-Almeida, J.F. Middleton, and E.J.D. Campos. 2013. The seasonal circulation of the Eastern Brazilian shelf between 10 ∘ S and 16 ∘ S: A modelling approach. *ContShelf Res* 65: 121–140. https://doi.org/10.1016/j.csr.2013.06.008.

Barton, E.D., J.L. Largier, R. Torres, M. Sheridan, A. Trasviña, A. Souza, Y. Pazos, and A. Valle-Levinson. 2015. Coastal upwelling and downwelling forcing of circulation in a semi-enclosed bay: Ria de Vigo. *Progresss in Oceanography.* https://doi.org/10.1016/j.pocean.2015.01.014.

Becherer, J., H. Burchard, G. Flöser, V. Mohrholz, and L. Umlauf. 2011. Evidence of tidal straining in well-mixed channel flow from microstructure observations. *Geophysical Research Letters* 38: L17611. https://doi.org/10.1029/2011GL049005.

Benazzouz, A., S. Mordane, A. Orbi, M. Chagdali, K. Hilmi, A. Atillah, J. Lluís Pelegrí, and D. Hervé. 2014. An improved coastal upwelling index from sea surface temperature using satellite-based approach - The case of the Canary Current upwelling system. *Continental Shelf Research.* https://doi.org/10.1016/j.csr.2014.03.012.

Berkelmans, R., S.J. Weeks, and C.R. Steinberga. 2010. Upwelling linked to warm summers and bleaching on the Great Barrier Reef.

Limnology and Oceanography. https://doi.org/10.4319/lo.2010.55.6.2634.

Castro, B.M., and L.B. Miranda. 1998. Physical oceanography of the western Atlantic continental shelf located between 4°N and 34°S, in: Robinson, A.R., Brink, K.H. (Eds.), *The Sea: The Global Coastal Ocean-Regional Studies and Syntheses*. USA. 209–251.

Cirano, M., and G.C. Lessa. 2007. Oceanographic Characteristics of Baía de Todos os Santos, Brazil. *Revista Brasileira de Geofísica*. https://doi.org/10.1590/S0102-261X2007000400002.

De Silva Samarasinghe, J.R., L. Bode, and L.B. Mason. 2003. Modelled response of Gulf St Vincent (South Australia) to evaporation, heating and winds. *Continental Shelf Research*. https://doi.org/10.1016/S0278-4343(03)00129-8.

Defant, A. 1961. *Physical Oceanography*. Pergamon Press 2.

Duxbury, A.C. 1979. Upwelling and estuary flushing. *Limnology and Oceanography* 24 (4): 627–633.

Edson, J.B., V. Jampana, R.A. Weller, S.P. Bigorre, A.J. Plueddemann, C.W. Fairall, S.D. Miller, L. Mahrt, D. Vickers, and H. Hersbach. 2013. On the Exchange of Momentum over the Open Ocean. *Journal of Physical Oceanography*. https://doi.org/10.1175/JPO-D-12-0173.1.

Egbert, G.D., and S.Y. Erofeeva. 2002. Efficient inverse modeling of barotropic ocean tides. *Journal of Atmospheric and Oceanic Technology*. https://doi.org/10.1175/1520-0426(2002)019%3c0183:EIMOBO%3e2.0.CO;2.

Geyer, W.R., and P. MacCready. 2014. The estuarine circulation. *Annual Reviews of Fluid Mechanics*. https://doi.org/10.1146/annurev-fluid-010313-141302.

Giddings, S.N., and MacCready, P. 2017. Reverse Estuarine Circulation Due to Local and Remote Wind Forcing, Enhanced by the Presence of Along-Coast Estuaries. *Journal of Geophysical Research Oceans*. https://doi.org/10.1002/2016JC012479.

Gilcoto, M., J.L. Largier, E.D. Barton, S. Piedracoba, R. Torres, R. Graña, F. Alonso-Pérez, N. Villacieros-Robineau, and F. de la Granda. 2017. Rapid response to coastal upwelling in a semienclosed bay. *Geophysical Research Letters*. https://doi.org/10.1002/2016GL072416.

Hansen, D.V., and M. Rattray. 1965. Gravitational Circulation in Straits and Estuaries. *Journal of Marine Research*. 23: 104–122.

Harcourt-Baldwin, J.L., and Diedericks, G.P.J. 2006. Numerical modelling and analysis of temperature controlled density currents in Tomales Bay, California. *Estuarine Coastal and Shelf Science*. https://doi.org/10.1016/j.ecss.2005.10.001.

Hickey, B.M., X. Zhang, and N. Banas. 2002. Coupling between the California Current System and a coastal plain estuary in low riverflow conditions. *Journal of Geophysical Research Oceans*. https://doi.org/10.1029/1999jc000160.

Juarez, B., A. Valle-Levinson and C. Li. 2020. Estuarine salt-plug induced by freshwater pulses from the inner shelf. *Estuarine Coastal and Shelf Science*. https://doi.org/10.1016/j.ecss.2019.106491.

Kämpf, J., and P. Chapman. 2016. Upwelling Systems of the World A Scientific Journey to the Most Productive Marine Ecosystems. *Springer International Publishing*. https://doi.org/10.1007/978-3-319-42524-5.

Lessa, G.C., R. Mariani, and L. Fonseca. 2019. Variability of the Thermohaline Field in a Large Tropical. *Well-Mixed Estuary: THe Influence of an Extreme Draught Event. Estuaries and Coasts*. https://doi.org/10.1007/s12237-019-00641-y.

Lessa, G.C., M.F.L. Souza, P.O. Mafalda D.F., Jr. Gomes, C.S. Souza, C.E. P. Teixeira, J.R.L.B. Souza, and M.R. Zucchi. 2018. Variabilidade Intra-anual da oceanografia da Baía de Todos os Santos: evidencias de tres anos de monitoramento, in: Hatje, V., Dantas, L.M.V., Andrade, J.B. de (Eds.), *Baia de Todos Dos Santos: avanços nos estudos de longo prazo*. EdUFBA, 158–192.

Lü, X., F. Qiao, C. Xia, J. Zhu, and Y. Yuan. 2006. Upwelling off Yangtze River estuary in summer. *Journal of Geophysical Research Oceans*. https://doi.org/10.1029/2005JC003250.

Mariani, R., G.C. Lessa, and M. Marta-Almeida. 2021. Long-term variability of the salinity field in a large tropical, well-mixed estuary: The influence of climatic trends. *Estuaries and Coasts*. https://doi.org/10.1007/s12237-021-01008-y.

Marta-Almeida, M., G.C. Lessa, A.L. Aguiar, F.N. Amorim, and M. Cirano. 2019. Realistic modelling of shelf-estuary regions: A multi-corner configuration for Baía de Todos os Santos. *Ocean Dynamics*. https://doi.org/10.1007/s10236-019-01304-z.

Marta-Almeida, M., M. Cirano, C. Guedes Soares, and G.C. Lessa. 2017. A numerical tidal stream energy assessment study for Baía de Todos os Santos, Brazil. *Renewable Energy*. https://doi.org/10.1016/j.renene.2017.01.047.

Monteiro, P.M.S., and J.L. Largier. 1999. Thermal stratification in Saldanha Bay (South Africa) and subtidal, density-driven exchange with the coastal waters of the Benguela upwelling system. *Estuarine Coastal and Shjelf Science*. https://doi.org/10.1006/ecss.1999.0550.

Palóczy, A., I.C.A. da Silveira, B.M. Castro, and L. Calado. 2014. Coastal upwelling off Cape São Tomé (22°S, Brazil): The supporting role of deep ocean processes. *Continental Shelf Research*. https://doi.org/10.1016/j.csr.2013.09.005.

Rueda-Roa, D.T., and F.E. Muller-Karger. 2013. The southern Caribbean upwelling system: Sea surface temperature, wind forcing and chlorophyll concentration patterns. *Deep Sea Research Part I: Oceanographic Research Papers*. https://doi.org/10.1016/j.dsr.2013.04.008.

Saha, S., S. Moorthi, H.L. Pan, X. Wu, Jiande Wang, S. Nadiga, P. Tripp, R. Kistler, J. Woollen, D. Behringer, H. Liu, D. Stokes, R. Grumbine, G. Gayno, Jun Wang, Y.T. Hou, H.Y. Chuang, H.M.H. Juang, J. Sela, M. Iredell, R. Treadon, D. Kleist, P. Van Delst, D. Keyser, J. Derber, M. Ek, J. Meng, H. Wei, R. Yang, S. Lord, H. Van Den Dool, A. Kumar, W. Wang, C. Long, M. Chelliah, Y. Xue, B. Huang, J.K. Schemm, W. Ebisuzaki, R. Lin, P. Xie, M. Chen, S. Zhou, W. Higgins, C.Z. Zou, Q. Liu, Y. Chen, Y. Han, L. Cucurull, R.W. Reynolds, G. Rutledge, and M. Goldberg. 2010. *The NCEP climate forecast system reanalysis*. Bull: American Meteorological Society. https://doi.org/10.1175/2010BAMS3001.1.

Santana, R., Teixeira, C., and Lessa, G. 2018. The Impact of Different Forcing Agents on the Residual Circulation in a Tropical Estuary (Baía de Todos os Santos, Brazil). *Journal of Coastal Research*. https://doi.org/10.2112/JCOASTRES-D-17-00044.1.

Santos, F.M., G.C. Lessa, M. Cirano, R.M. Domingues, and C.A.D. Lentini. 2014. Localized coastal upwelling at the Brazil Current formation zone (13°S). *Proc. 17th Brazilian Syposium on remote Sensing*. http://www.dsr.inpe.br/sbsr2015/files/p0892.pdf. Accessed 17 Jan 2023.

Shchepetkin, A.F., and J.C. McWilliams. 2005. The regional oceanic modeling system (ROMS): A split-explicit, free-surface, topography-following-coordinate oceanic model. *Ocean Modeling*. https://doi.org/10.1016/j.ocemod.2004.08.002.

Sun, Y.J., I. Jalón-Rojas, X.H. Wang, and D. Jiang. 2018. Coastal upwelling by wind-driven forcing in Jervis Bay, New South Wales: A numerical study for 2011. *Estuarine, Coastal and Shelf Science*. https://doi.org/10.1016/j.ecss.2017.11.022.

Tapia, F.J., S.A. Navarrete, M. Castillo, B.A. Menge, J.C. Castilla, J. Largier, E.A. Wieters, B.L. Broitman, and J.A. Barth. 2009. Thermal indices of upwelling effects on inner-shelf habitats. *Progress in Oceanography*. https://doi.org/10.1016/j.pocean.2009.07.035.

Thévenin, M.R., J. Pereira, and G.C. Lessa. 2019. Shelf-break upwelling on a very narrow continental shelf adjacent to a western boundary current formation zone. *Journal of Marine System*. https://doi.org/10.1016/j.jmarsys.2019.02.008.

Trenberth, K.E., J.C. Olson, and W.G. Large. 1989. A Global Ocean Wind Stress Climatology Based on ECMWF Analyses. Technical

Report NCAR/TN-338+STR, National Center for Atmospheric Research, Boulder, Colorado, 98. https://opensky.ucar.edu/islandora/object/technotes%3A107/datastream/PDF/download/A_Global_Ocean_Wind_Stress_Climatology_Based_on_ECMWF_Analyses.citation.

Valle-Levinson, A., L.P. Atkinson, D. Figueroa, and L. Castro. 2003. Flow induced by upwelling winds in an equatorward facing bay: Gulf of Arauco, Chile. *Journal of Geophysical Research Ocean*. https://doi.org/10.1029/2001JC001272.

Wallcraft, A.J., E.J. Metzger, S.N. Carroll. 2009 Design description for the HYbrid Coordinate Ocean Model (HYCOM) version 2.2. Tech. rep. Naval Research Laboratory, Stennins Space Center, MS.